

MASK EFFECTS ON COSMOLOGICAL STUDIES WITH WEAK LENSING PEAK STATISTICS

XIANGKUN LIU, ZUHUI FAN

Department of Astronomy, Peking University, Beijing 100871, China; fanzuhui@pku.edu.cn

Draft version April 11, 2013

ABSTRACT

In this paper, we analyze in detail with numerical simulations how the bad data removal, i.e., the mask effect, can influence the peak statistics of the weak lensing convergence field reconstructed from the shear measurement of background galaxies. It is found that high peak fractions are systematically enhanced due to the presence of masks, the larger the masked area, the higher the enhancement. In the case that the total masked area is about 13% of the survey area, the fraction of peaks with signal-to-noise ratio $\nu \geq 3$ is $\sim 13\%$ of the total number of peaks, in comparison with $\sim 9\%$ of the mask-free case in our considered cosmological model. This can have significant effects on cosmological studies with weak lensing convergence peak statistics, inducing a large bias in the parameter constraints if the effects are not taken into account properly. Even for a survey area of 9 deg^2 , the bias in (Ω_m, σ_8) is already intolerably large and close to 3σ . It is noted that most of the affected peaks are close to the masked regions. Therefore excluding peaks in those regions in the peak statistics can reduce the bias effect but at the expense of losing usable survey areas. Further investigations find that the enhancement of the number of high peaks around the masked regions can be largely attributed to the fewer number of galaxies usable in the weak lensing convergence reconstruction leading to higher noise than that of the areas away from the masks. Based on Fan et al. (2010), we thus develop a two-noise-level model that treats the areas close to and away from the masked regions separately. It is shown that the model can account for the mask effect on peak statistics very well, and the bias in cosmological parameters is significantly reduced if this model is applied in the parameter fitting. We also analyze the systematic effects on peak statistics resulting from the nonlinear convergence reconstruction, including the smoothing order problem and the mass-sheet degeneracy.

Subject headings: cosmology - dark matter - clusters: general - gravitational lensing: weak - large-scale structure of universe

1. INTRODUCTION

Gravitationally induced weak lensing effects have emerged as one of the most important probes in cosmological studies (e.g., Bartelmann & Schneider 2001; Albrecht et al. 2006; Amendola et al. 2012; Abate et al. 2012; Heymans et al. 2012; Erben et al. 2012; Simpson et al. 2012; Kilbinger et al. 2012). Besides the shear two-point correlation analyses, weak lensing peak statistics can provide important and complementary information especially considering that the structure formation is a nonlinear process (e.g., White et al. 2002; Hamana et al. 2004; Tang & Fan 2005; Hennawi & Spergel 2005; Marian et al. 2009; Dietrich & Hartlap 2010; Kratochvil et al. 2010; Marian et al. 2012; Hilbert et al. 2012). Current generation of observations have proved the feasibility of detecting massive clusters from weak lensing peak identifications (e.g., Wittman et al. 2006; Gavazzi & Soucail 2007; Shan et al. 2012). Future weak lensing surveys will be able to provide a large number of peaks with high signal-to-noise ratio and therefore their statistics should expectedly be able to contribute significantly to precision cosmological studies. On the other hand, it is known that many effects can affect profoundly the weak lensing peak statistics. The complex mass distribution of clusters of galaxies and the projection effects of large-scale structures along line of sights prevent us from linking weak lensing peaks to single clusters in a simple way (e.g., Tang & Fan 2005; Yang et al. 2011; Yang et al. 2012; Hamana et al. 2012). The intrinsic ellipticities of source galaxies generate large noise that not only produces false peaks through their chance alignments (e.g., Van Waerbeke 2000; Fan 2007) but also affects the true peak signals from massive clusters

significantly (Fan et al. 2010). Furthermore, various observational effects can also have large impacts on weak lensing peak statistics if they are not taken into account properly. The full realization of the power of weak lensing analyses in future cosmological studies relies on our thorough understandings about different systematics.

Weak lensing observations target at far way background galaxies, and bad data occurrences are unavoidable and they should be masked out carefully (e.g., Heymans et al. 2012; Erben et al. 2012). These masks can occupy $\sim 10\%$ to $\sim 20\%$ of the total survey area and result irregular survey boundaries and artificial voids in the background galaxy distribution, which in turn can affect the weak lensing analyses considerably. In Hikage et al. (2011), they investigate the mask effect on the shear power spectrum estimation and propose the pseudo-spectrum method to account for the effect. Considering convergence peaks, because the convergence field is reconstructed from the shape measurements of background galaxies, the devoidness of galaxies in masked regions affects the convergence calculation and consequently the peak statistics inevitably. In this paper, we perform detailed studies about the mask effect on weak lensing convergence peak statistics and further the derived cosmological parameter constraints. We adopt the simulations from White & Vale (2004) as the fiducial inputs for weak lensing signal calculations. Background galaxies with intrinsic ellipticities are randomly populated and ‘observed’ ellipticities including the shear signals from the fiducial inputs are then constructed for each galaxies. The masks are generated according to the mask size distribution from Shan et al. (2012), and are given spatial positions randomly in our statistical analyses. We then

remove galaxies inside the masks and reconstruct the convergence field from remaining galaxies. The peak statistics is analyzed and compared with the case without masks. We further explore different methods to correct the mask effects. Along the way, we also analyze the systematic effects arising from the nonlinear convergence reconstruction on peak statistics.

The rest of the paper is organized as follows. In §2, we introduce the basics related to our studies, including the convergence reconstruction method and the theoretical peak model of Fan et al. (2010) used in our analyses. In §3, we describe the different simulations constructed for our analyses and the procedures for cosmological parameter fitting assuming the peak counts from simulations as the ‘observational data’. The main results are presented in §4. Discussions are given in §5.

2. THEORETICAL BASICS

2.1. Convergence reconstruction

Observationally, the weak lensing effect is mostly extracted from the shape distortion measurements of background galaxies, which is directly related to the weak lensing shear components. On the other hand, the lensing convergence is the weighted projection of the density distribution along the line of sight, and thus more visually linked to the structures we are interested in. In this paper, we concentrate on the convergence peak analyses.

Considering small source galaxies, their linear-order image distortion from the gravitational lensing effect of a single lens can be described by the Jacobian matrix given by (e.g., Schneider et al. 1992)

$$A = \left(\delta_{ij} - \frac{\partial^2 \psi(\theta)}{\partial \theta_i \partial \theta_j} \right) = \begin{pmatrix} 1 - \kappa - \gamma_1 & -\gamma_2 \\ -\gamma_2 & 1 - \kappa + \gamma_1 \end{pmatrix}, \quad (1)$$

where κ is the lensing convergence and γ_1 and γ_2 are the two shear components with

$$\kappa = \frac{1}{2} \nabla^2 \psi, \quad \gamma_1 = \frac{1}{2} \left(\frac{\partial^2 \psi}{\partial \theta_1^2} - \frac{\partial^2 \psi}{\partial \theta_2^2} \right), \quad \gamma_2 = \frac{\partial^2 \psi}{\partial \theta_1 \partial \theta_2}. \quad (2)$$

The lensing potential ψ is determined by the surface mass density of the lens through

$$\psi(\theta) = \frac{1}{\pi} \int d^2 \theta' \frac{\Sigma(\theta')}{\Sigma_{cr}} \ln |\theta - \theta'|, \quad (3)$$

where Σ_{cr} is the critical surface mass density given by

$$\Sigma_{cr} = \frac{c^2}{4\pi G} \frac{D_s}{D_l D_{ls}} \quad (4)$$

with D_l , D_s and D_{ls} being the angular diameter distances from the observer to the lens, to the source, and between the lens and the source. It can be seen that $\kappa = \Sigma/\Sigma_{cr}$. For weak lensing effects from large-scale structures beyond a single lens, under the Born approximation the above formulations still hold except the lensing convergence is given by, in the case of a fixed source position (e.g., Bartelmann & Schneider 2001),

$$\kappa_{eff} = \frac{3H_0^2 \Omega_m}{2c^2} \int_0^w dw' \frac{f_K(w') f_K(w - w')}{f_K(w)} \frac{\delta[f_K(w') \theta, w']}{a(w')}, \quad (5)$$

where w is the comoving radial distance, f_K is the angular diameter distance, a is the scale factor of the universe, and δ is the density perturbation along the line of sight.

The image distortion is then described by κ and γ_i with the quantity $(\det A)^{-1} = [(1 - \kappa)^2 - |\gamma|^2]^{-1}$ giving rise to the flux

magnification ($|\gamma| = (\gamma_1^2 + \gamma_2^2)^{1/2}$), and the eigen values of A related to the axial length. Specifically, the lensing effect makes a circular source appear as an ellipse with the axial ratio of

$$\frac{a^2}{b^2} = \frac{1 - \kappa - |\gamma|}{1 - \kappa + |\gamma|} = \frac{1 - |g|}{1 + |g|}, \quad (6)$$

where $g_i = \gamma_i/(1 - \kappa)$ is named as the reduced shear component. Thus for ideally circular sources, we can obtain g by accurately measuring the shape of the sources, and further reconstruct the convergence κ from the relation between κ and γ , which in the Fourier space can be written as (e.g., Kaiser & Squires 1993)

$$\hat{\gamma}(l) = \pi^{-1} \hat{D}(l) \hat{\kappa}(l), \quad (7)$$

where \hat{D} is given by

$$\hat{D}(l) = \pi \frac{l_1^2 - l_2^2 + 2il_1 l_2}{|l|^2}. \quad (8)$$

However, galaxies have intrinsic ellipticities. The complex ellipticity of the lensing distorted image ϵ with $|\epsilon| = (1 - b/a)/(1 + b/a)$ is then related to the intrinsic ones ϵ_s by the following relation (e.g., Seitz & Schneider 1997)

$$\epsilon = \begin{cases} \frac{\epsilon_s - g}{1 - g^* \epsilon_s} & \text{for } |g| \leq 1 \\ \frac{1 - g \epsilon_s^*}{\epsilon_s^* - g^*} & \text{for } |g| > 1 \end{cases} \quad (9)$$

It has been shown that the average of ϵ gives rise to the unbiased estimate of g and $1/g$ for $|g| \leq 1$ and $|g| > 1$, respectively (Seitz & Schneider 1997). We further construct the distortion δ by (e.g., Schneider & Seitz 1995)

$$\delta = \frac{2\langle \epsilon \rangle}{1 + |\langle \epsilon \rangle|^2} = \frac{2g}{1 + |g|^2} \quad (10)$$

as the observed quantity, which is independent of $|g| \leq 1$ or > 1 . One can then solve for γ by

$$\gamma = \frac{1 - \kappa}{\delta^*} [1 \pm \sqrt{1 - |\delta|^2}], \quad (11)$$

where the sign is determined by $-\text{sign}[\det(A)]$. We proceed the reconstruction of the lensing convergence iteratively from the following relation

$$\kappa(\theta) = -\frac{1}{\pi} \int_{R^2} d^2 \theta' \text{Re}[D(\theta - \theta') \gamma^*(\theta')] \quad (12)$$

where $D(\theta) = (\theta_1^2 - \theta_2^2 + 2i\theta_1 \theta_2)/|\theta|^4$. Specifically, we start by assuming $\kappa^{(0)} = 0$ and $|g| \leq 1$ everywhere, and thus (e.g., Bartelmann 1995)

$$\gamma^{(0)}(\theta) = \frac{1 - \sqrt{1 - |\delta(\theta)|^2}}{\delta^*(\theta)}. \quad (13)$$

At n -th step, we obtain $\kappa^{(n)}$ from $\gamma^{(n-1)}$ via Eq.(12) and further calculate $\gamma_{test}^{(n)}$ from $\kappa^{(n)}$ to determine the sign of $\det(A^{(n)})$ everywhere. At $n+1$ step, we insert $\kappa^{(n)}$ into Eq. (11) to estimate $\gamma^{(n)}$ by considering the signs of $\det(A^{(n)})$ calculated in step n .

In the case of $\kappa \ll 1$ and $|\gamma| \ll 1$, we have $\langle \epsilon \rangle = -g \approx -\gamma$, and thus the convergence reconstruction is a single-step linear process.

2.2. Peak model

To constrain cosmological parameters from weak lensing peak abundances, we need to calculate the expected peak numbers for different cosmological models. From previous section, we see that the intrinsic ellipticities of lensed galaxies are the dominant source of errors in weak lensing analyses. With the process of averaging over a number of galaxies to obtain the estimate of the lensing signal, the residual noise is on the order of $\sigma_\epsilon / \sqrt{n_g \theta_G^2}$, where σ_ϵ is the rms of the intrinsic ellipticities, n_g is the surface number of lensed galaxies in the weak lensing analyses, and θ_G is the smoothing scale used in the averaging. Such a noise can affect significantly the weak lensing peak statistics. In our studies here, we employ the theoretical model of Fan et al. (2010) to calculate peak numbers for relatively high peaks in cosmological parameter fittings. The model takes into account the effects of noise by considering the noise-induced bias and the dispersion on the height of the true convergence peaks from massive halos and the enhancement of the noise peak abundances due to the existence of the true mass distribution properly.

Specifically, the model assumes that the derived convergence field after a smoothing can be written as $K_N = K + N$, where K represents the true lensing convergence, and N is for the residual noise from intrinsic ellipticities. The noise field N is modeled as a Gaussian random field from the central limit theorem (e.g., Van Waerbeke 2000). The model concentrates on high peaks and assumes that true peaks come from individual massive halos. Thus a considered area is split into halo regions and field regions. In an individual halo region, the peak number distribution can be calculated from the Gaussian statistics of K_N with known K from the halo. Then the total number of peaks in halo regions can be obtained from the summation of the peaks in halo regions weighted by the halo mass function. In the field region, the numbers of peaks are directly computed from the noise field N . The total surface number density of peaks is then written as

$$n_{peak}(\nu) d\nu = n_{peak}^c(\nu) d\nu + n_{peak}^n(\nu) d\nu, \quad (14)$$

where $\nu = K_N / \sigma_0$ is the signal-to-noise ratio of a peak and the term $n_{peak}^c(\nu)$ is for halo regions including both true peaks corresponding to real halos and the noise peaks within the halo regions, and $n_{peak}^n(\nu)$ is for field regions with only noise peaks. For $n_{peak}^c(\nu)$, We have

$$n_{peak}^c(\nu) = \int dz \frac{dV(z)}{dz d\Omega} \int dM n(M, z) f(\nu, M, z), \quad (15)$$

where $dV(z)$ is the cosmological volume element at redshift z , $d\Omega$ is the solid angle element, $n(M, z)$ is the mass function of dark matter halos and,

$$f(\nu, M, z) = \int_0^{R_{vir}} dR (2\pi R) n_{peak}(\nu, R, M, z) \quad (16)$$

gives rise to the number of peaks in the area within the virial radius of a halo of mass M at redshift z . Here $n_{peak}(\nu, R, M, z)$ describes the surface number density of peaks at the location of R from the center of the halo, which depends on the projected density profile of dark matter halos and is given by Eq.(15) of Fan et al. (2010). We adopt the Sheth-Tormen mass function in our calculations (Sheth & Tormen 1999). The linear power spectrum used in computing the rms density perturbations is the same as that used in the simulations

of White & Vale (2004) from Eisenstein & Hu (1999). The NFW profile (Navarro et al. 1996, 1997) is applied to describe the density distribution of dark matter halos with the concentration-mass relation given by Bullock et al. (2001)

$$c_{vir}(M, z) = \frac{c_*}{1+z} \left(\frac{M}{10^{14} h^{-1} M_\odot} \right)^{-0.13}, \quad (17)$$

where c_* is taken to be $c_* = 8$. The field term $n_{peak}^n(\nu)$ is given by

$$n_{peak}^n(\nu) = \frac{1}{d\Omega} \left\{ n_{ran}(\nu) \left[d\Omega - \int dz \frac{dV(z)}{dz} \times \int dM n(M, z) (\pi R_{vir}^2) \right] \right\}, \quad (18)$$

where $n_{ran}(\nu)$ is the surface number density of pure noise peaks (Fan et al. 2010).

3. SIMULATIONS AND COSMOLOGICAL PARAMETER FITTING FROM PEAK WEAK LENSING PEAK COUNTS

3.1. Base simulations

In our analyses, we use a set of lensing maps constructed from a flat Λ CDM N-body simulation by White & Vale (2004) as our base inputs. The cosmological parameters of the considered simulation are $\Omega_m = 0.296$, $h = 0.7$, $\sigma_8 = 0.93$, and $n = 1$, where Ω_m and h are the present dimensionless matter density of the universe and the Hubble constant in units of $100 \text{ km s}^{-1} \text{ Mpc}^{-1}$, respectively, σ_8 is the rms of the extrapolated linear density perturbations smoothed over $8 h^{-1} \text{ Mpc}$, and n is the power index of the initial power spectrum of density fluctuations. The N-body simulation box is $200 h^{-1} \text{ Mpc}$, and the force softening length is $\sim 30 h^{-1} \text{ kpc}$. The simulation starts from $z = 50$, and the initial conditions are generated from the transfer function for the power spectrum given by Eisenstein & Hu (1999) with the baryonic oscillations smoothed out (White & Vale 2004). Two sets of simulations are done with different realizations of the initial conditions. The lensing convergence and shear are calculated through the ray-tracing technique. The source redshift is set to be $z_s = 1$. With 16 from each simulation, we have total 32 sets of $3 \times 3 \text{ deg}^2$ convergence and shear maps constructed along different line of sights (White & Vale 2004), and each has 1024×1024 pixels. They form the base data sets for our weak lensing peak studies. It is noted that the cosmological parameters are in accord with WMAP1 (e.g., Spergel et al. 2003) and different somewhat from the most recent fitting results, especially for σ_8 (e.g. Komatsu et al. 2011; Hinshaw et al. 2012). However, because we mainly focus on analyzing mask effects by comparing weak lensing peak statistics with and without masks, the choice of cosmological model should not affect our results significantly.

3.2. Fiducial reconstructed convergence maps

To analyze weak lensing convergence peaks, previous studies often add a Gaussian noise arising from intrinsic ellipticities directly to convergence maps from N-body simulations to construct ‘observed’ maps (e.g., Hamana et al. 2004a; Tang & Fan 2005; Yang et al. 2012). Observationally however, a convergence map has to be reconstructed from the measured galaxy ellipticities. To mimic observations, we thus also perform the convergence reconstruction. We generate source

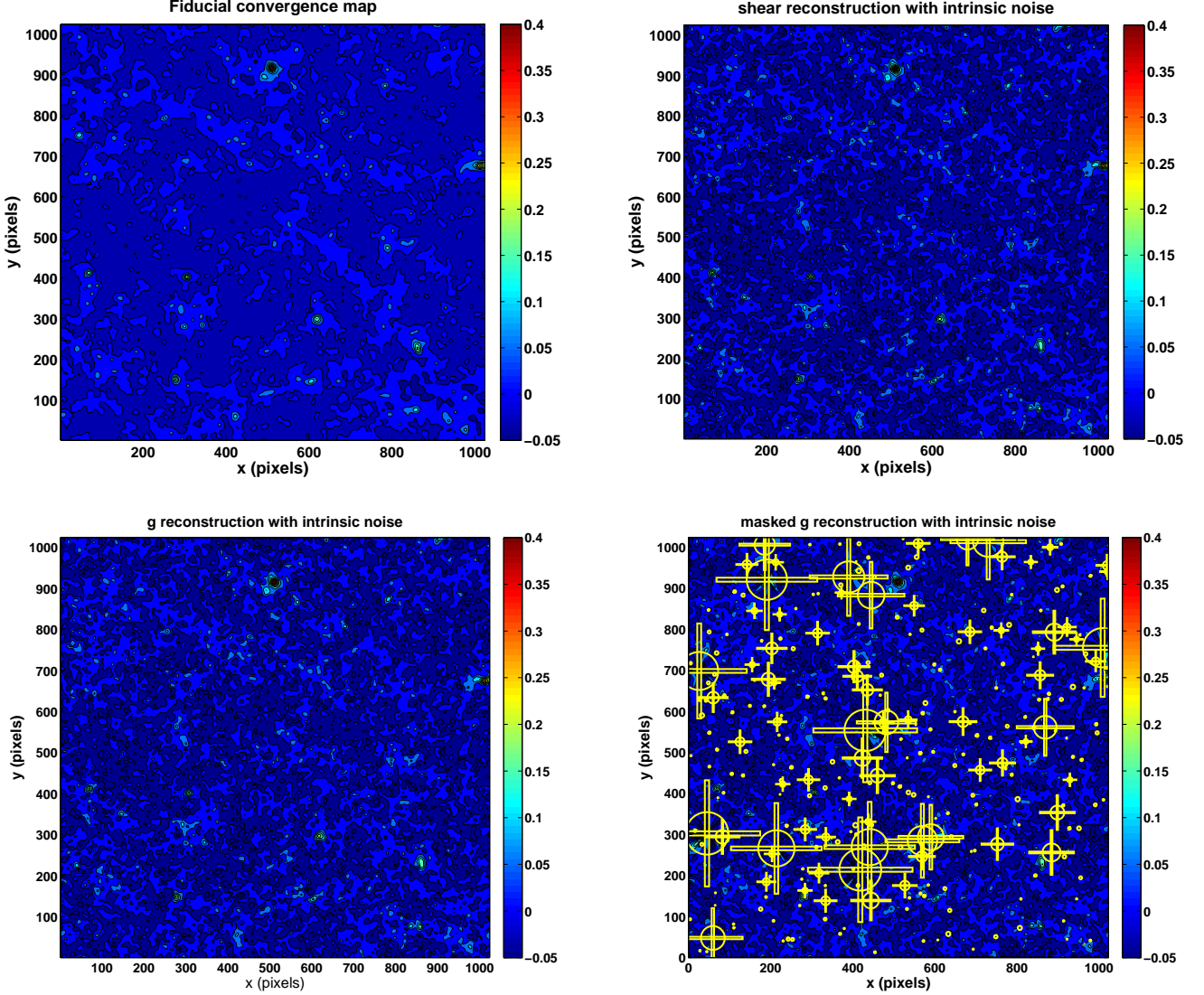


Figure 1. Upper-Left: One example of the smoothed base convergence map without noise; Upper-Right: The corresponding shear reconstructed convergence map with intrinsic ellipticities of source galaxies included; Lower-Left: The corresponding g reconstructed convergence map; Lower-Right: The corresponding masked g reconstructed convergence map, here the yellows are the masks in this case.

galaxy catalogs by randomly populating them in angular positions at $z_s = 1$ and assigning them intrinsic ellipticities according to the following probability distribution

$$p_s(\epsilon_{s1}, \epsilon_{s2}) = \frac{\exp[-(\epsilon_{s1}^2 + \epsilon_{s2}^2)/\sigma_\epsilon^2]}{\pi\sigma_\epsilon[1 - \exp(-1/\sigma_\epsilon^2)]}, \quad |\epsilon_s| \in [0, 1] \quad (19)$$

where ϵ_{s1} and ϵ_{s2} are the two components of the intrinsic ellipticities, $|\epsilon_s| = \sqrt{\epsilon_{s1}^2 + \epsilon_{s2}^2}$ and the rms dispersion of $|\epsilon_s|$ is taken to be $\sigma_\epsilon = 0.4$. We assume the number density of source galaxies to be $n_g = 30 \text{ arcmin}^{-2}$, and the spatial clustering and the intrinsic alignment of source galaxies are not considered here. We calculate the reduced shear signal \mathbf{g} for each source galaxy from the base pure lensing maps by interpolation from regular grids to galaxy positions. The ‘observed’ galaxy ellipticities ϵ are then constructed according to Eq.(9). We calculate the average $\langle \epsilon \rangle$ on positions of regular grids as

follows

$$\langle \epsilon \rangle(\theta) = \frac{\sum_i W(\theta_i - \theta) \epsilon(\theta_i)}{\sum_i W(\theta_i - \theta)}, \quad (20)$$

where the summation is over galaxy positions represented by the subscript i . The window function W is taken to be Gaussian given by

$$W(\mathbf{x}) = \frac{1}{\pi\theta_G^2} \exp\left(-\frac{|\mathbf{x}|^2}{\theta_G^2}\right). \quad (21)$$

The smoothing scale θ_G is set to be $\theta_G = 1 \text{ arcmin}$. With the obtained $\langle \epsilon \rangle$, the convergence reconstruction is done iteratively as described in §2.1. The results converge quickly with about eight iterations for the converging accuracy of 10^{-6} . For each base map, we generate 5 sets of galaxy catalogs with different realizations of spatial positions and intrinsic ellipticities. We thus obtain total of $32 \times 5 = 160$ reconstructed $3 \times 3 \text{ deg}^2$ convergence maps. We refer such maps as ‘ g reconstruction’. For comparison, we also generate sets of ‘ob-

served' ellipticities by $\epsilon = \epsilon_s - \gamma$ and perform linear reconstruction to get convergence maps, which are referred to as 'shear reconstruction' maps.

Figure 1 shows a set of convergence maps. The upper left is the base pure convergence map smoothed with a Gaussian window function with $\theta_G = 1$ arcmin. The upper right and lower left are the reconstructed maps from shear and from the reduce shear g , respectively. We can see that the reconstructed maps are noisy comparing to the base one, but most of the high peaks are still apparent. On the other hand, the noise affects the peak height and the pure noise peak distribution is also biased by the true mass distribution, which have to be taken into account properly in modeling the weak lensing peak statistics (Fan et al. 2010). The two reconstructed maps from shear and from g are very similar, but there are subtle systematic differences, for which we will discuss later in §4. The lower right map is the reconstruction with masks to be described in the next subsection.

3.3. Mask model and convergence reconstruction with masks

Removing bad/low quality imaging data is essential in weak lensing observational analyses. This leaves holes in the source galaxy distribution, which in turn affects the convergence reconstruction and subsequent cosmological studies. To investigate the mask effects on weak lensing peak counts statistically, we generate mock masks by modeling the basic masks for point sources, bright saturated stars and bad pixels being circular in shape. The mask size distribution is in accord with that of CFHTLS used in Shan et al. (2012). We also add rectangle-shaped masks in both x and y directions to those circular ones with radius larger than 1 arcmin to mask out saturation spikes. These extra masks have a size of $0.2r \times 5r$ with r being the radius of the circular mask to be added on. We populate masks randomly in each of the considered $3 \times 3 \text{ deg}^2$ fields. With the size distribution of Shan et al. (2012), the total number of masks in each field is set to be N_{mask} . We consider three cases with $N_{\text{mask}} = 140, 280$, and 420 , corresponding to the total masked area fraction of $\sim 6\%$, $\sim 13\%$ and $\sim 19\%$, respectively. We then remove galaxies within masks from the source galaxy catalogs generated in §3.2 and reconstruct convergence maps from the remaining source galaxies. An example is shown in the lower right panel of Figure 1. The masks are shown in yellow. We then have two separate sets of convergence maps reconstructed from 'observed' ellipticities without and with masks, respectively, and each set contains totally 160 of $3 \times 3 \text{ deg}^2$ convergence maps for peak analyses.

3.4. Cosmological parameter constraints

The mask effects on cosmological studies with weak lensing peak statistics are investigated by analyzing their impacts on cosmological parameter constraints from weak lensing peak counts. As described in §2.2, Fan et al. (2010) propose a model to calculate the peak counts including both the true peaks from massive halos and noise peaks from chance alignment of background galaxies by taking into account the influence of noise on true peaks and the noise peak enhancement due to the mass distribution around halos properly. The model allows us to use directly the number of peaks detected from 'observed' convergence maps for cosmological studies without the need to identify true peaks associated with massive halos. It should be pointed out that the model of Fan et al. (2010) is built on the assumption that true peaks are associated with individual dark matter halos. It has been shown

that this is largely valid for high peaks (e.g., Yang et al. 2011). For low peaks, on the other hand, the projection effect from large scale structures along line of sights is significant. We are in the process developing a more complete model including the projection effects. With that, the cosmological constraints from peak counts can be extended to include low peaks to further enhance the cosmological gains. At the moment, however, we only concentrate on high peaks. For the noise level considered here, we include peaks with $3.75 \leq \nu \leq 6.75$ in the analyses, where the signal-to-noise ratio of peaks is defined as $\nu = K_N/\sigma_0$ with σ_0 the rms of noise from intrinsic ellipticities. In the Gaussian smoothing used here, $\sigma_0 = \sigma_\epsilon/(4\pi n_g \theta_G^2)^{1/2}$ (e.g. van Waerbeke 2000). For $\sigma_\epsilon = 0.4$, $n_g = 30 \text{ arcmin}^{-2}$ and $\theta_G = 1$ arcmin, we have $\sigma_0 = 0.02$. The high-end cut is introduced to avoid the possible bias from the very limited number of highly massive halos existed in the relatively small-sized simulations we used.

We construct the 'observed data' specifically as follows. For each of the considered case, we have 160 of $3 \times 3 \text{ deg}^2$ convergence maps. To reduce the boundary effects on peak counts, we exclude the outermost 10 pixels in each direction in peak counting. Thus the effective area of each map is $[3(1 - 20/1023)]^2 \approx 8.65 \text{ deg}^2$. For each map, we count peaks in 6 signal-to-noise ratio bins of width 0.5 in the range of $3.75 \leq \nu \leq 6.75$. We further obtain the mean number of peaks in each bin by averaging over the 160 maps. We then scale the peak counts back to 9 deg^2 by multiplying a factor of $9/8.65$ on the peak counts in each bins. These peak counts form the 'observed' data denoted by \bar{N}_i ($i = 1, \dots, 6$). For cosmological parameter fitting, we also calculate the covariance matrix by

$$C_{ij} = \frac{1}{R-1} \sum_{r=1}^R (N_i^{(r)} - \bar{N}_i)(N_j^{(r)} - \bar{N}_j), \quad (22)$$

where r denotes different maps and $R = 160$. The parameter constraints are then obtained by minimizing the χ^2 defined by

$$\chi_{f'}^2 = dN^{(f')}(C)^{-1}dN^{(f')} = \sum_{ij=1,\dots,6} dN_i^{(f')}(C_{ij}^{-1})dN_j^{(f')}, \quad (23)$$

where $dN_i^{(f')} = N_i^{(f')} - \bar{N}_i$ with $N_i^{(f')}$ being the model prediction for the cosmological model f' .

4. RESULTS

As described previously, we use the model of Fan et al. (2010) as the basic theoretical model. Thus before presenting the mask effects, we first need to show the cosmological applicability of the model. Although it has been demonstrated that the model works well for high peak counts (Fan et al. 2010), here we test the model applicability quantitatively by performing cosmological parameter constraints from the 'observed' peak counts without masks. Along the way, we also discuss the effects of reconstruction on peak counts. With these analyses results, we then proceed to discuss the mask effects.

4.1. The model applicability in cosmological parameter constraints

To exam the model applicability and possible effects arising from convergence reconstruction, we construct separate sets of 'observed data' from convergence maps obtained by different ways. In the very weak lensing regime, the observed

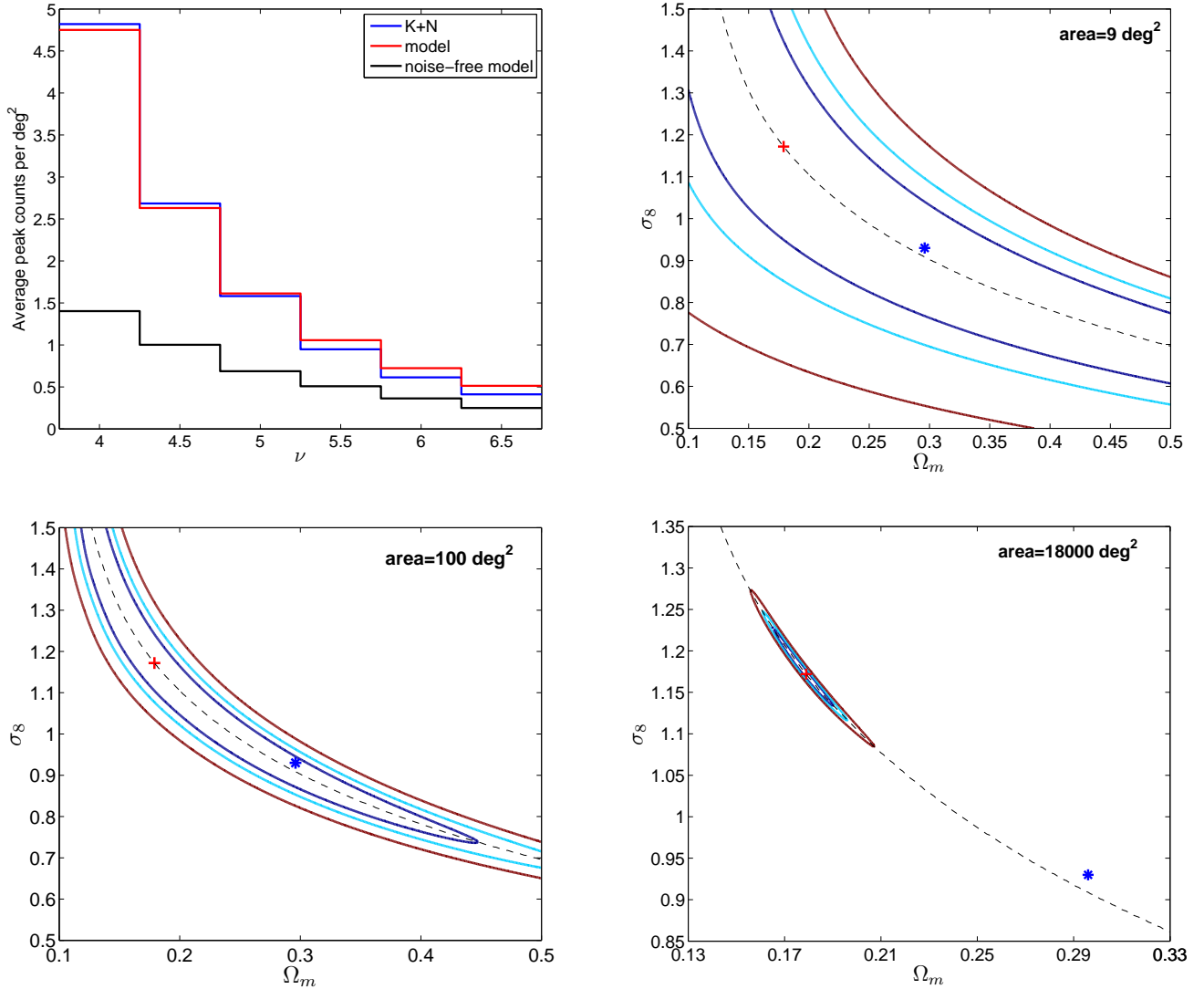


Figure 2. Upper-Left: The average peak counts in 1 deg^2 . The blue, red and black histograms are for the results from direct noise-added convergence maps, from the model prediction, and from the noise-free base convergence maps. Upper-Right: Cosmological constraints on (Ω_m, σ_8) from χ^2 fitting for a survey area of 9 deg^2 for the direct noise-added case. The solid lines are 1σ , 2σ and 3σ confidence contours. The blue symbol represents the fiducial input parameters of the simulations and the red symbol is the best-fit result. The dashed line shows the best fit σ_8 given Ω_m and represents more or less the direction of the degeneracy of the two parameters. Lower-Left: Same as the upper-right panel but for the survey area $S = 100 \text{ deg}^2$. Lower-Right: Same as the upper-right one, but for the survey area $S = 18,000 \text{ deg}^2$.

ellipticity for a background galaxy can be written as $\epsilon \approx \epsilon_s - \gamma$, and consequently, the reconstructed convergence after a suitable smoothing is $K_N = K + N$ where K is the smoothed lensing convergence and N is the residual noise due to the finite-number averaging of the intrinsic ellipticities of source galaxies, which is approximately Gaussian due to the central limit theorem (e.g., van Waerbeke 2000). Therefore a straightforward way to include the noise from intrinsic ellipticities into consideration is to linearly add the noise field N directly to the base convergence maps from simulations. This approach has been adopted by many previous numerical studies on weak lensing peak statistics (e.g., Hamana et al. 2004a; Tang & Fan 2005; Yang et al. 2012). As discussed in §2.2, the form of $K_N = K + N$ is also the starting point of the model of Fan et al. (2010). We thus first construct a set of noisy convergence maps by adding a random Gaussian noise to the 1024×1024

grids of the base convergence maps with the variance given by (e.g., Hamana et al. 2004a)

$$\sigma_{pix}^2 = \frac{\sigma_\epsilon^2}{2} \frac{1}{n_g \theta_{pix}^2}, \quad (24)$$

where $\sigma_\epsilon = 0.4$, $n_g = 30 \text{ arcmin}^{-2}$, and $\theta_{pix} = 180/1024 \text{ arcmin}$ is the angular size of a pixel. We then smooth the noise-add convergence maps with a Gaussian smoothing of $\theta_G = 1 \text{ arcmin}$. We generate 5 noisy convergence maps with different realizations of the noise field, and perform peak counting from the total of 160 convergence maps to obtain the first set of ‘observed data’ and the corresponding covariance matrix. Note that the model of Fan et al. (2010) is a spherical halo-based model with only noise effects included. Thus by carrying out cosmological parameter fitting to this set of ‘observed data’, we can test if other effects

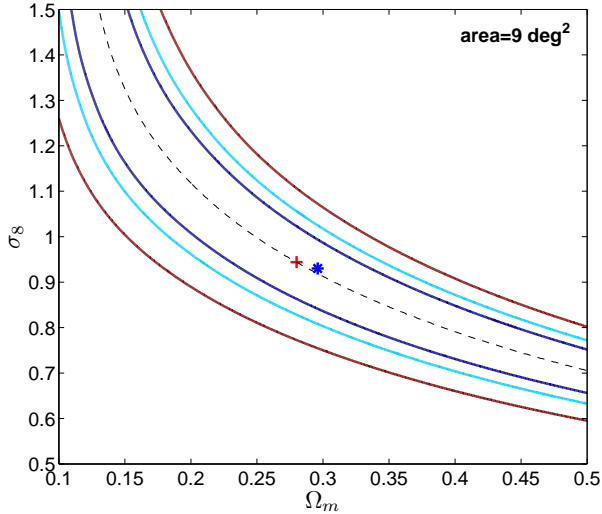


Figure 3. Cosmological parameter constraints from χ^2 fitting for 9 deg² shear reconstruction case. The lines and symbols are the same as those in the upper right panel of Figure 2.

beyond the noise from intrinsic ellipticities, e.g., the projection effects from large-scale structures and the non-sphericity of dark matter halos, can affect weak lensing peak counts and therefore bias the fitting result significantly.

The fitting results are presented in Figure 2. The upper left panel shows the peak counts per deg² from the noisy convergence maps (blue), the Fan et al.’s model prediction (red) and the peak counts from base convergence maps without noise. It is seen that the existence of noise systematically increases the number of peaks due to its influence on true peak heights and the number enhancement of pure noise peaks around dark matter halo regions (Fan et al. 2010). The model prediction agrees with the results from noisy convergence maps quite well. It is noted that the base convergence maps are generated from two sets of N-body simulations with the box size of $200h^{-1}\text{Mpc}$. Because of the relatively small simulation box, the number of massive dark matter halos is limited and the sample variance can be significant. Although we have excluded the very high peaks in the consideration, the peak counts from the two sets of 16 base convergence maps from two different realizations of the simulations are apparent. This sample variance contributes dominantly to the differences between the blue and the red histograms at high ends. The good agreement between the model prediction and the ‘observed data’ shows that the noise effects from intrinsic ellipticities of background galaxies are the leading systematics for weak lensing peak counts in the considered range and the projection effects and the non-sphericity of dark matter halos play minor roles statistically. The upper right panel shows the fitting result with the observed area of 9 deg². The covariance matrix used in the fitting is calculated directly from the 160 noisy convergence maps. The blue symbol is the fiducial parameter input of the simulation with $\Omega_m = 0.293$ and $\sigma_8 = 0.93$, and the red symbol is the best fit based on the model of Fan et al. (2010). The solid lines from inside out are the 1σ , 2σ and 3σ contours, respectively. The dotted line shows the best fit σ_8 given Ω_m and represents more or less the degeneracy between the two cosmological parameters with respect to the peak counts considered here. The location of the best fit

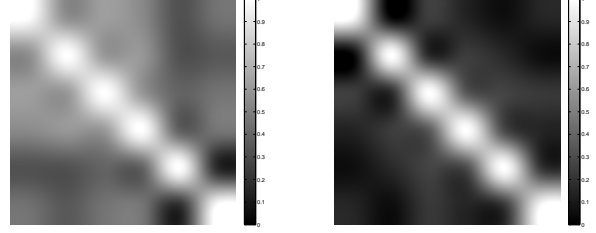


Figure 4. The normalized covariance matrix in grey scale for the direct noise-added case (left) and for the shear reconstruction case (right).

(Ω_m, σ_8) along the dotted line changes somewhat from one set of runs to another, again owing to the degeneracy of the two parameters and the χ^2 differs only slightly along the dotted line. The fact that the blue symbol is very close to the dotted line shows that the model used in the parameter fitting works well without introducing significant bias. We also consider the cases with the survey area of 100 deg² and 18000 deg² shown in the lower left and lower right panels, respectively. We take a simple approach to rescale the covariance matrix calculated from 160 noisy convergence maps to the two larger surveys assuming a Poisson scaling relation to the survey area S as $1/S$ (Kratochvil et al. 2010). This may underestimate the covariance matrix by a factor of ~ 1.5 given the existence of long-range correlations of the true peaks (Kratochvil et al. 2010). Furthermore, for our analyses here, the base convergence maps are derived from only two sets of simulations with a relatively small simulation box. Thus the sample variance cannot be averaged out, which affects the ‘observed’ peak counts as shown in the upper left panel of Figure 2. This also leads to an underestimate of the covariance matrix. Keeping these in mind, the fitting result for $S = 100 \text{ deg}^2$ is still good without significant bias comparing to the statistical errors. For the case with $S = 18000 \text{ deg}^2$, the best fit values are away from the fiducial inputs significantly in a statistical sense. Thus for future precision cosmological studies, we need to further develop our model to take into account more effects in addition to the noise effects. On the other hand, as discussed above, to fully quantify the model performance, we also need larger simulations so that the sample variance bias can be well controlled and the covariance matrix can be suitably estimated.

The main focus of the paper is to investigate the mask effects on weak lensing peak counts. For that purpose, we conclude that the model of Fan et al. (2010) is good enough to reveal the bias on cosmological parameter fitting induced by the mask effects because of their significance (see §4.2).

To be more close to observational analyses, we also construct two sets of ‘observed data’ and the corresponding covariance matrix from convergence maps obtained from shear reconstruction and reduced-shear g reconstruction, respectively. For the shear reconstruction described in §3.2, we artificially generate ‘observed ellipticities’ of source galaxies by $\epsilon = \epsilon_s - \gamma$ and then reconstruct the convergence maps linearly. Mathematically, we expect that the obtained convergence maps should be exactly the same as $K_N = K + N$. The fitting result is shown in Figure 3. Noting the approximate degeneracy of the two parameters along the dotted line, the best fit result is indeed very consistent with that shown in the upper right panel of Figure 2. However, the confidence contours here are considerably tighter. Shown in Figure 4,

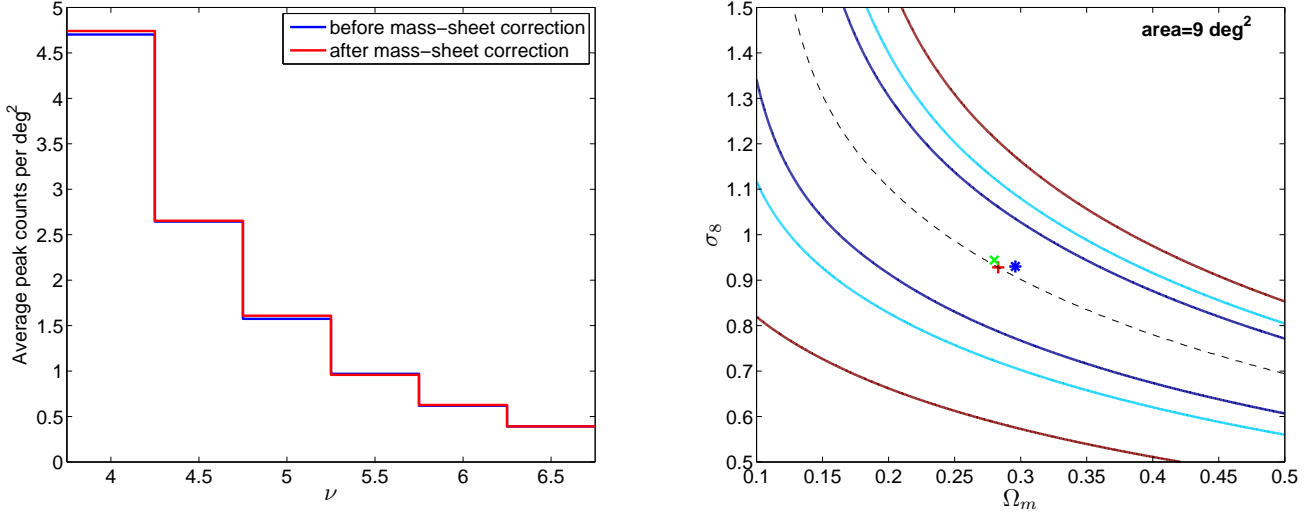


Figure 5. The left panel shows the average peak counts before (blue) and after (red) the mass-sheet correction for the shear reconstruction case. The right panel shows the corresponding cosmological parameter constraints after the correction. The blue, red and green symbols represent the fiducial input of the simulations, the best fit after and before the mass-sheet correction, respectively.

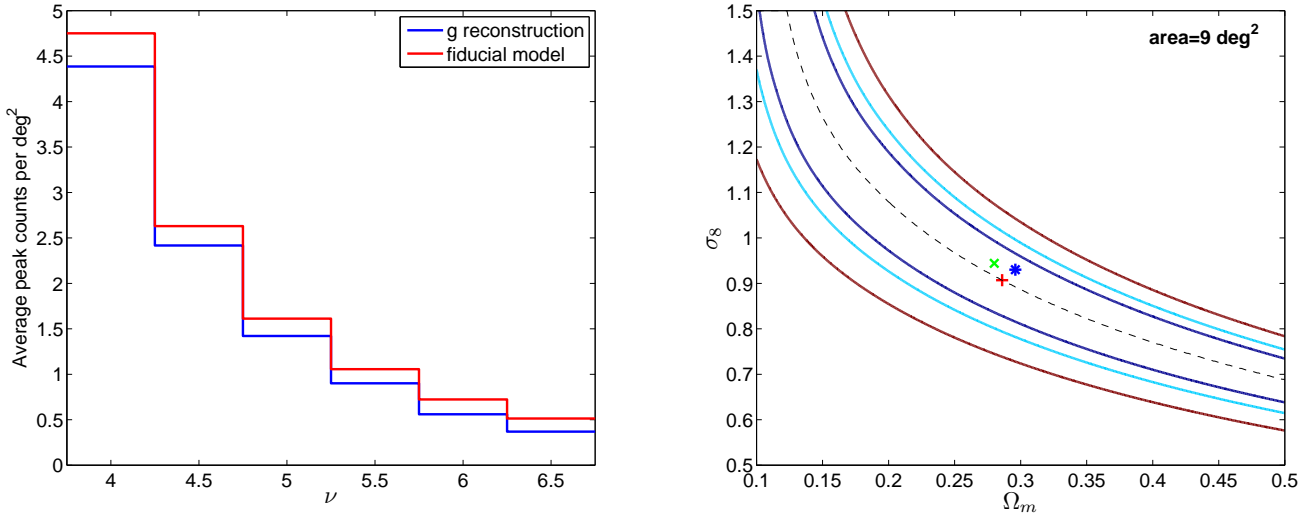


Figure 6. The results for the g reconstruction case. The left panel shows the average peak counts with the blue one from g reconstructed maps and the red one for the theoretical predictions. The right panel shows the corresponding cosmological constraints. The red, green and blue symbols are the best fit from the g reconstruction, the shear reconstruction and the fiducial input, respectively.

we exam the covariance matrices from the direct noise-added maps (left) and the shear reconstructed maps (right), and find that the cross correlations are much smaller in the latter case. Careful analyses show that this difference is due to the mass-sheet degeneracy inherited from the reconstruction. In the reconstruction case, the average $\langle K_N \rangle = 0$ over the whole map. For the direct noise-added case, however, $\langle K_N \rangle \approx \langle K \rangle$. For a region of $3 \times 3 \text{ deg}^2$, the true average K is on the order of 10^{-3} and different maps have different $\langle K \rangle$. The fluctuations in $\langle K \rangle$ lead to larger cross correlations in the covariance matrix calculated from the direct noise-added maps than that in the reconstruction case with $\langle K_N \rangle = 0$ for all the maps. On the other hand, because the fluctuations in $\langle K \rangle$ can be either positive or negative, there is no net effect on the average peak counts. To demonstrate this, we make corrections to each shear reconstructed map by adding the value $\langle K \rangle$ of the correspond-

ing base convergence map to it and then perform the peak counting and calculate the covariance matrix. The results are shown in Figure 5, where the left panel shows the average peak counts from shear reconstructed maps before (blue) and after correction (red), and the right panel shows the parameter constraints from the corrected shear reconstructed maps with the blue symbol for the fiducial input, the red symbol for the best fit from the corrected maps and the green one for the best fit from the uncorrected shear reconstructed maps. It is seen that the confidence contours are indeed enlarged and are very much the same as that of the upper right panel of Figure 2. It should be pointed out that this mass-sheet degeneracy effect depends on the considered survey areas, the larger the area, the weaker the effect.

We now turn to the results from g reconstruction, which mimics the observational analyses the most. The results are

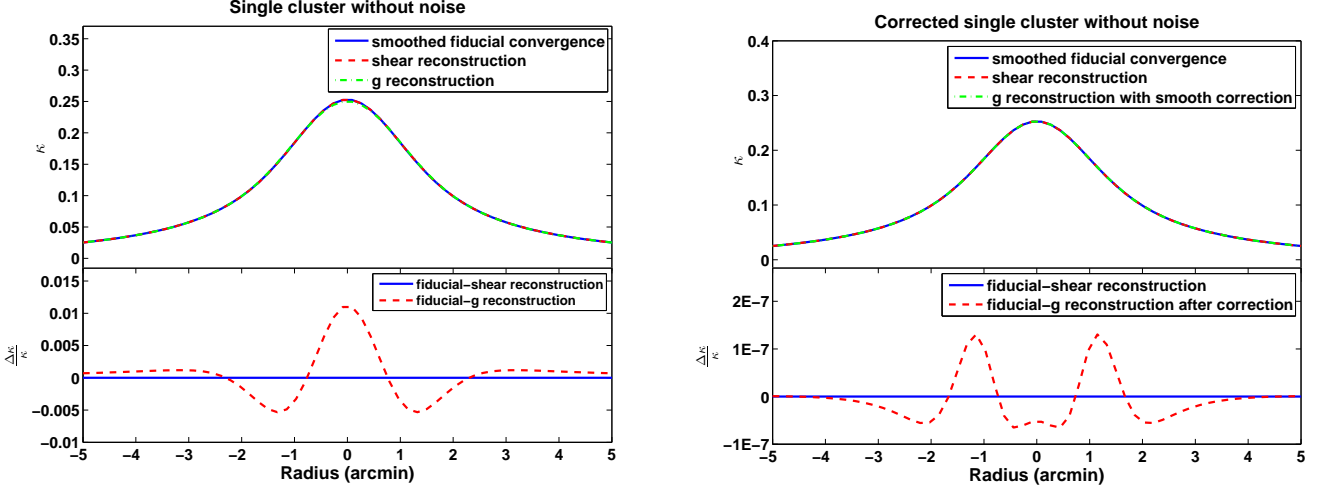


Figure 7. Test results for a known dark matter halo. The upper left panel shows the smoothed convergence profiles from theoretical calculations (solid blue), the shear reconstruction (dashed red) and the g reconstruction (dash-dotted green), respectively. The right panels are the same as the left one except the g reconstruction results are corrected. The lower left panel shows the corresponding relative differences.

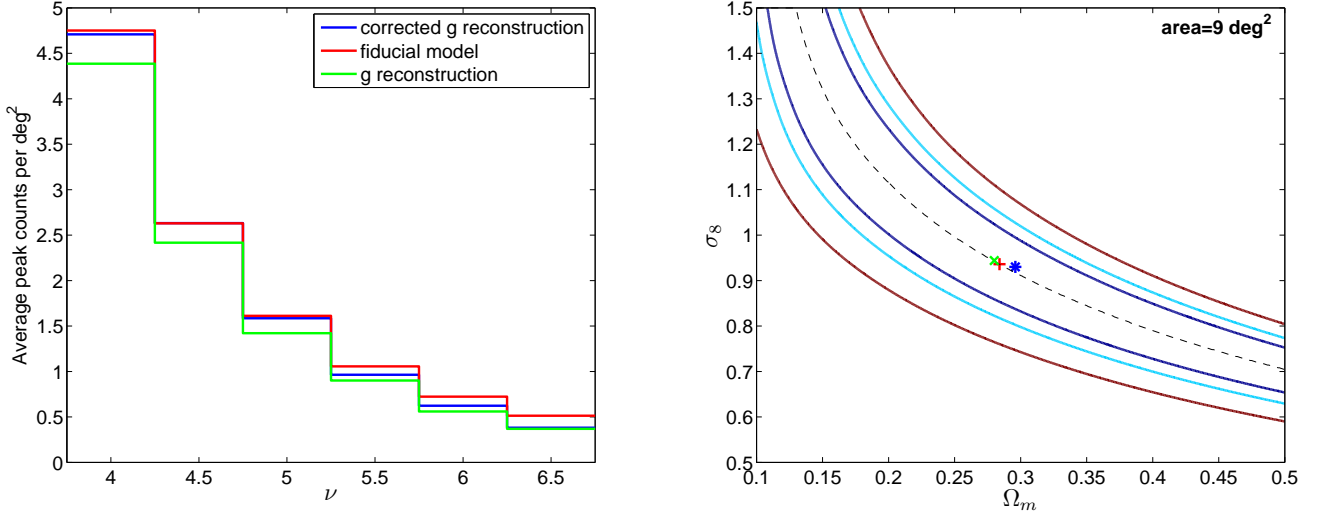


Figure 8. Similar to Figure 6, but for the results of corrected g reconstruction.

shown in Figure 6. The left panel presents the average peak counts from the g -reconstructed maps (blue) and the model prediction of Fan et al. (2010). It is seen that the blue histogram is systematically lower than the red one. This is also reflected in the cosmological parameter fitting shown in the right panel. The fiducial input (blue symbol) is clear above the degeneracy dotted line where the best fit (red) is on although the difference is still well within the 1σ range here. For comparison, we also show the best fit from the shear reconstruction case (green symbol), which is closer to the fiducial input considering the degeneracy of the two parameters (see Figure 3). Similar to the shear reconstruction case, here the mass sheet degeneracy also causes apparently tighter confidence levels than those of the direct noise-added case.

For the systematically lower peak counts from g reconstruction, we find that it results largely from the smoothing in g . As we described in §3.2, to carry out the reconstruction, we first need to obtain a local estimate of g by averaging (smoothing) over surrounding source galaxies. Such a procedure gives rise

to $\langle g \rangle = \langle \gamma / (1 - \kappa) \rangle$ (in the sub-critical case with $|g| < 1$), but not $\langle \gamma \rangle / (1 - \langle \kappa \rangle)$. Consequently, the reconstructed convergence is not the same as the real smoothed convergence. Specifically, the real smoothed convergence should be mathematically obtained by

$$\begin{aligned} \langle \kappa(\vec{x}) \rangle = & -\frac{1}{\pi} \int_{R^2} d^2 \vec{x}' (1 - \langle \kappa(\vec{x}') \rangle) \\ & \times \text{Re} [D(\vec{x} - \vec{x}') \frac{\langle \gamma^*(\vec{x}') \rangle}{1 - \langle \kappa(\vec{x}') \rangle}]. \end{aligned} \quad (25)$$

The difference between $\langle g \rangle$ and $\langle \gamma \rangle / (1 - \langle \kappa \rangle)$ (denoted by α) leads to the difference between the g reconstructed convergence (denoted as $\langle \kappa_g \rangle$ for the moment) and the real $\langle \kappa \rangle$. Let $\Delta x = \langle \kappa_g \rangle - \langle \kappa \rangle$, we then have, to the linear order in α and Δx ,

$$\Delta x = -\frac{1}{\pi} \int_{R^2} d^2 \vec{x} \text{Re}\{D(\vec{x} - \vec{x}')\} \times \left[[1 - \langle \kappa(\vec{x}') \rangle] \alpha^* - \Delta x \frac{\langle \gamma^*(\vec{x}') \rangle}{1 - \langle \kappa(\vec{x}') \rangle} \right]. \quad (26)$$

We demonstrate this smoothing order problem by considering the weak lensing signal from a single known NFW dark matter halo with mass of $M = 10^{15} M_\odot$. The left panels of Figure 7 show the results by setting the intrinsic ellipticities of source galaxies to be zero to isolate the smoothing order problem. The upper panel shows the smoothed convergence profiles from the theoretical calculations (solid blue), the shear reconstruction (dashed red) and the g reconstruction (dash-dotted green), respectively. The lower panel gives the relative differences between the theoretical result and the results from shear reconstruction (blue) and the g reconstruction (dashed red), respectively. It is seen that while there is almost no difference for the shear reconstruction case, the relative difference is on the order of 1% in the central region of the halo in the g reconstruction case. This results the peak height from g reconstruction to be lower than the theoretical one by $0.01\langle \kappa_0 \rangle$. Because the dark matter halo is known, we can calculate α , and further to get Δx iteratively. The right panels of Figure 7 show the corrected results for g reconstruction. We can see that after the correction, the difference between the theoretical calculation and that from the g reconstruction decreases to the order of 10^{-7} . We notice that with the noise from intrinsic ellipticities included, the correction due to the smoothing order problem gets larger. For our peak counts analyses here, we have the base shear and convergence maps. Therefore we can construct the direct noise-added shear and convergence fields and then calculate α at each grid point. With the α field, the correction Δx at each grid point can be obtained. The corrected results are shown in Figure 8. The blue histogram is for the corrected peak counts, which is very consistent with the results from either the direct noise-added convergence maps (upper left panel of Figure 2) or the shear reconstructed maps (left panel of Figure 5), and is in good agreement with the model prediction (red histogram). The green histogram is for the uncorrected peak counts. The right panel shows the parameter constraints from the corrected peak counts. The meaning of the symbols and lines are the same as that in the right panel of Figure 6. It is seen that the best fit values (red symbol) are very close to the best fit from the shear reconstruction (green symbol) and agree with the fiducial ones (blue symbol) very well. Thus for clarity, in the following discussions of the mask effects, we use the corrected convergence maps from g reconstruction in both cases with and without masks.

It should be pointed out that in real observational analyses, we cannot perform such corrections for the smoothing order problem straightforwardly because we do not know the true signals. We will explore ways to handle such effects in our future studies.

4.2. Mask effects

In this section, we discuss the mask effects on weak lensing peak analyses by comparing two sets of g -reconstructed convergence maps corrected for the smoothing order problem with and without masks, respectively. There are totally 160 maps for each set. For each map in the case without masks, there is a corresponding map with masks that the

source galaxies are exactly the same as the other one except that the galaxies within the masked regions are discarded. We then have 160 pairs of maps that allow us to do detailed comparisons. The mask model is described in §3.3. Three cases with the number of masks $N_{\text{mask}} = 140, 280$ and 420 for each 9 deg^2 (corresponding mask fraction of $\sim 6\%$, $\sim 13\%$ and $\sim 19\%$, respectively) are considered and $N_{\text{mask}} = 280$ is taken to be our fiducial case for most of the results presented in the following.

To perform detailed studies for peaks in convergence maps with and without masks, we need to identify the peak correspondences between each pair of maps. This is done by peak matching. For each peak in a map from one set, we check for peaks within 3.5 arcmin in each dimension around it in its peer map from another set and define the nearest peak within this region as its partner peak. Only those pairs of peaks that are partners to each other are identified as peaks with correspondences.

4.2.1. Effects on weak lensing peak analyses

The existence of masks affects the convergence reconstruction and consequently the peak properties both in their spatial location and peak height.

In Figure 9 we present the mask effect on spatial positions of peaks for $N_{\text{mask}} = 280$. The left panel shows an example map of the spatial distribution of peaks with correspondences. The squared and plus symbols are respectively for peaks in the cases with and without masks. The red, black and yellow ones are for the pairs of peaks with their spatial offset larger than 0.5 arcmin, in the range of $[0.2, 0.5]$ arcmin and less than 0.2 arcmin, respectively. It is seen clearly that strongly affected peaks are almost all closely associated with masks, especially large masks. In the right panel of Figure 9, the statistical offset distribution averaged over 160 pairs of maps is shown. There are about 40% of peaks with offset larger than 0.1 arcmin. The fraction with offset larger than 0.5 arcmin is $\sim 11\%$. We also notice that lower peaks are more strongly affected by masks. This offset due to mask can have significant effects on weak lensing analyses for individual clusters. For a typical weak lensing observation targeting at a particular cluster, the observed size is about 20 arcmin. If there happens to be a large mask close to the central region of the cluster, the weak lensing determined center for the cluster can be considerably offsetted from its true center, which in turn can lead to large errors in the weak lensing determination of the density profile for the cluster.

We now discuss the mask effects on peak heights. Figure 10 shows the results, where the left panels are the peak number distribution in 9 deg^2 averaged over 160 maps in each case and the right panels are the peak number differences between the cases without and with masks. The upper and lower panels are for the peak height measured in K_N and in signal-to-noise ratio $\nu = K_N/\sigma_0$ with $\sigma_0 = 0.02$, respectively. It is clearly seen that the number of peaks in high signal-to-noise bins is systematically higher in the case with masks, which can expectedly affect the cosmological parameter constraints with weak lensing peak counts significantly. We further examine the correlation between the positions of the strongly affected peaks and the locations of masks. We define two types of strongly affected peaks. Type I is for peaks with their peak height difference between the cases with and without masks higher than 1σ . Type II is for peaks without correspondences between the two cases. Figure 11 presents a typical map with masks. The left panel shows the spatial distribution of peaks

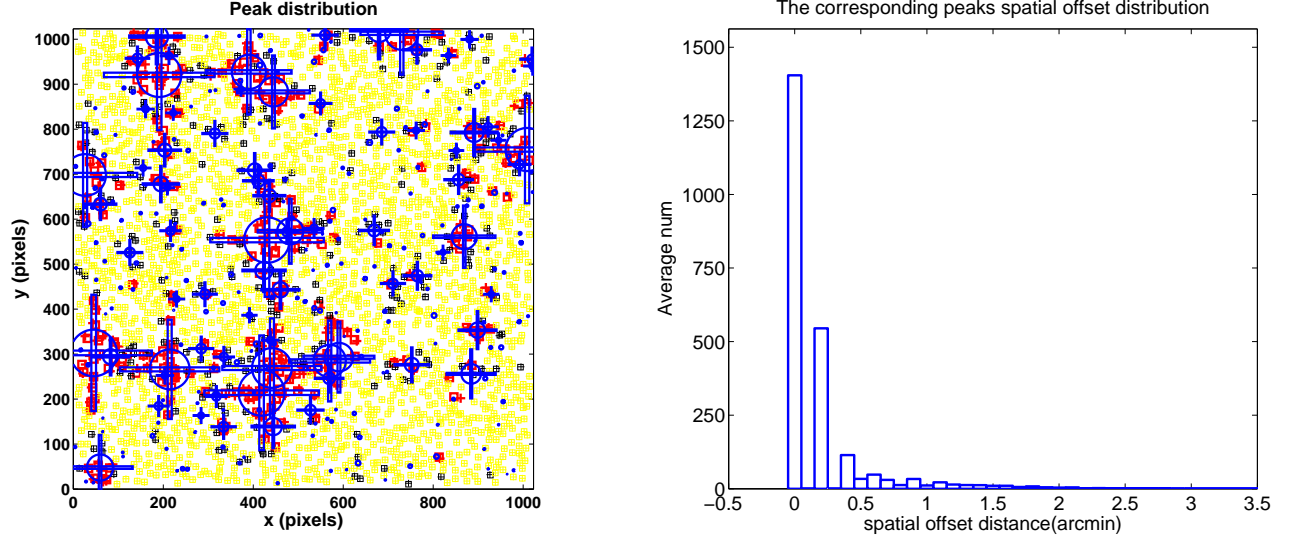


Figure 9. The mask effects on peak positions. The left panel shows the spatial distribution of peaks in one map. The square and plus symbols are for peaks in the case with and without masks, respectively. The red, black and yellow ones are, respectively, for peaks with spatial offsets larger than 0.5 arcmin, in the range of [0.2 arcmin, 0.5 arcmin] and less than 0.2 arcmin. The masks are shown in blue. The right panel is the statistical distribution of the spatial offset obtained by averaging over the 160 pairs of maps.

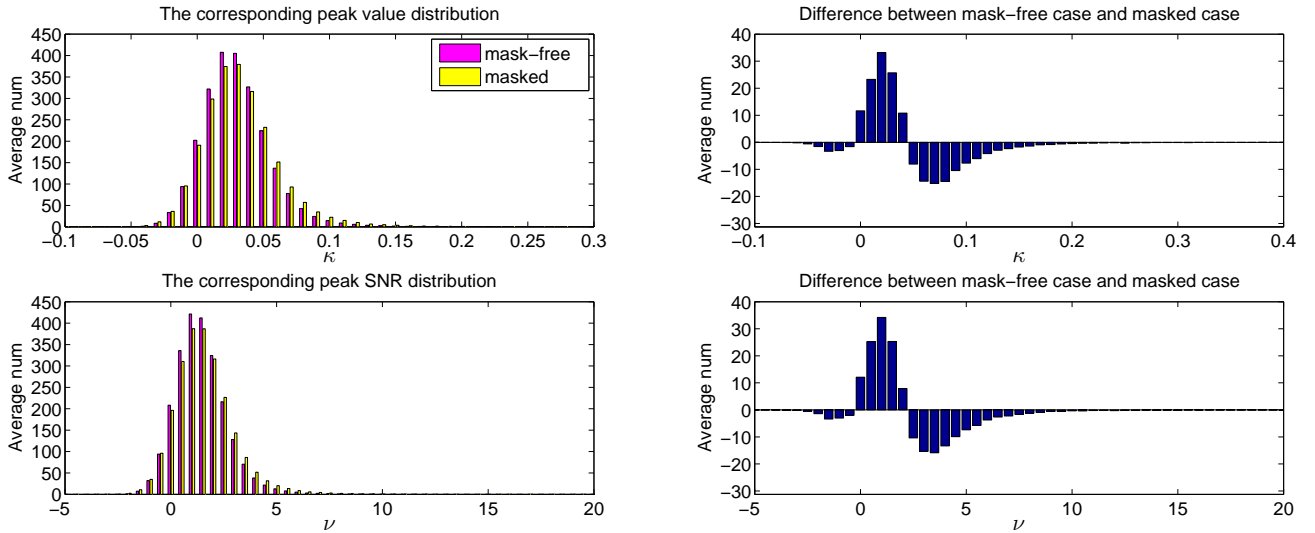


Figure 10. The peak counts distribution. The left panels show the peak number distributions for the cases with (yellow) and without (purple) masks. The right panels show the peak number difference between the case without and with masks. In the upper panels, the peak height is measured in K_N , and in the lower panels, it is measured in $\nu = K_N/\sigma_0$ with $\sigma_0 = 0.02$.

with squares and pluses for peaks in the cases with and without masks, respectively. The red symbols are for Type I peaks, the green symbols are for Type II peaks with the purple ones for Type II peaks with $\nu \geq 2$, and the yellow ones are for the rest. The clustering of the strong affected peaks around large masks are apparent. The right panel shows particularly the Type I peaks with $\nu < 3.25$ in the case without masks but with the corresponding peak height shifting to $\nu > 4.25$ in the case with masks. It is found that they all trace large masks. It is these high Type I peaks that can affect profoundly the cosmological parameter constraints discussed here.

Figure 12 shows the fitting results. The peak counts averaged over 160 maps in each case are shown in the upper left panel. The blue, green and red histograms are for peak counts in the case with masks, without masks and the theoret-

ical prediction of Fan et al. (2010) with a uniform noise with $\sigma_0 = 0.02$. It is seen clearly that the peak counts considered here are systematically larger due to the presence of masks. The upper right panel shows the fitting results with the survey area of 9 deg^2 . The fitting is done with the ‘observed data’ being the peak counts for the masked case, and the model of Fan et al. (2010) with $\sigma_0 = 0.02$. The meanings of the lines and symbols are similar to those of Figure 3. Clearly, the enhanced peak counts due to the occurrence of masks lead to a large bias in cosmological parameter fitting. Even for a survey of 9 deg^2 , the true cosmological parameter values (blue symbols) lie outside the 2σ contour around the best fit (red symbol). This demonstrates the significance of the mask effects, which must be taken into account carefully in cosmo-

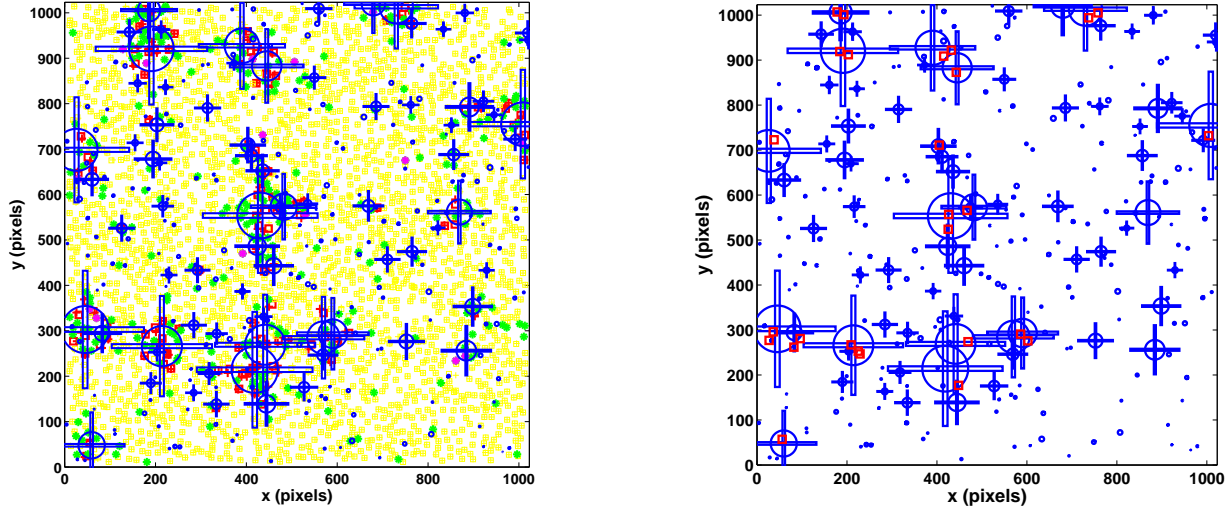


Figure 11. The illustration of the spatial distribution of the affected peaks. In the left panel, the red, green and purple symbols are for Type I affect peaks, Type II affected peaks and Type II with $\nu \geq 2$, respectively. The yellow symbols are for the rest of the peaks with correspondences between the case with and without masks. The right panel shows the Type I peaks with $\nu < 3.25$ in the case without masks but with the corresponding peak height shifting to $\nu > 4.25$ in the case with masks (red symbols).

logical parameter constraints with weak lensing peak counts. The lower left and right panels show the results for the survey areas of 100 deg^2 and 18000 deg^2 , respectively. The bias due to the mask effects is intolerable.

The above results are shown for the average masked area fraction of $\sim 13\%$ with $N_{\text{mask}} = 280$ in 9 deg^2 . We also analyze how the effects depend on the masked fraction. We consider three cases with the number of masks $N_{\text{mask}} = 140, 280$ and 420 in 9 deg^2 and the corresponding masked fraction of $\sim 6\%$, $\sim 13\%$ and $\sim 19\%$, respectively. The peak statistics are listed in Table 1. The mask effects are clearly stronger for larger masked fraction. The fraction of peaks with $\nu > 3$ is about 9% in the case without masks. This fraction increases to $\sim 11\%$, $\sim 13\%$ and $\sim 15.7\%$ for $N_{\text{mask}} = 140, 280$ and 420 , respectively. More than 90% and 70% of Type I and Type II affected peaks, respectively, are within the regions around masks with a size of twice the mask radius. The results are further visually illustrated in Figure 13 with all the symbols the same as those shown in left panel of Figure 11. The corresponding fitting results for the survey area of 9 deg^2 are shown in Figure 14. We see that with the increase of the masked fraction, the effects become larger. For the masked fraction of $\sim 19\%$, the bias for (Ω_m, σ_8) is already larger than 3σ for a 9 deg^2 survey.

4.2.2. Mask effects correction

We have demonstrated in §4.2 that the mask effects on weak lensing peak counts are significant. The subsequent cosmological parameter constraints are largely biased if they are not taken into account properly. We therefore need to explore ways for how to control the mask effects on cosmological applications with weak lensing peak counts.

From Table 1 and Figure 11, we see that the strongly affected peaks are mostly clustered around masks. Thus the first method we use to suppress the mask effects is to exclude the severely affected regions around masks when performing the peak counting. It is expected that the bias on cosmological parameters can be considerably removed but inevitably at

the expense of losing effective survey areas and therefore enlarging the statistical error contours. We name this method as the rejection method. We consider three cases with the rejection regions of 1, 1.5 and 2 times of the mask size around each mask. We pay attention to the mask overlaps. Figure 15 shows the results. The upper left panel shows the peak number distributions. The blue histogram is for the peak counts without applying rejection. The black one is for the peak counts after rejecting regions of 1.5 times of the mask size. The red one is the model prediction of Fan et al. (2010) with a uniform noise level of $\sigma_0 = 0.02$. All the peak counts are scaled to 1 deg^2 . The upper right, lower left and right show the fitting results for the three considered rejections, from the smallest to the largest rejections, respectively. It is seen that rejecting only the masked areas is not enough (upper left panel) and the bias is still apparent. With the rejection of regions of 1.5 times of the mask size around masks, the bias is suppressed to an insignificant level (lower left). To increase the rejection areas further does not improve the bias any more (lower right panel). It is also seen that with the increase of the rejection areas, the confidence contours become larger as expected. We thus conclude that to reject regions of 1.5 times of mask size around masks is an optimal choice that can remove the bias in cosmological parameter constraints without losing statistics significantly.

We now consider another approach in which we still keep the regions around masks in the peak counting. Here however, the regions around masks and the regions away from masks must be theoretically considered differently. In other words, we need to revise our theoretical model. The major difference between the two types of regions is the effective number of galaxies that can be used in the convergence reconstruction. In regions around masks, much fewer galaxies are usable. Therefore the noise level in those regions is systematically higher. This higher noise affects the peak counts in regions around masks in two ways. One is that the systematic peak height shift for true peaks is larger than regions away from masks (Fan et al. 2010). The other is the enhancement

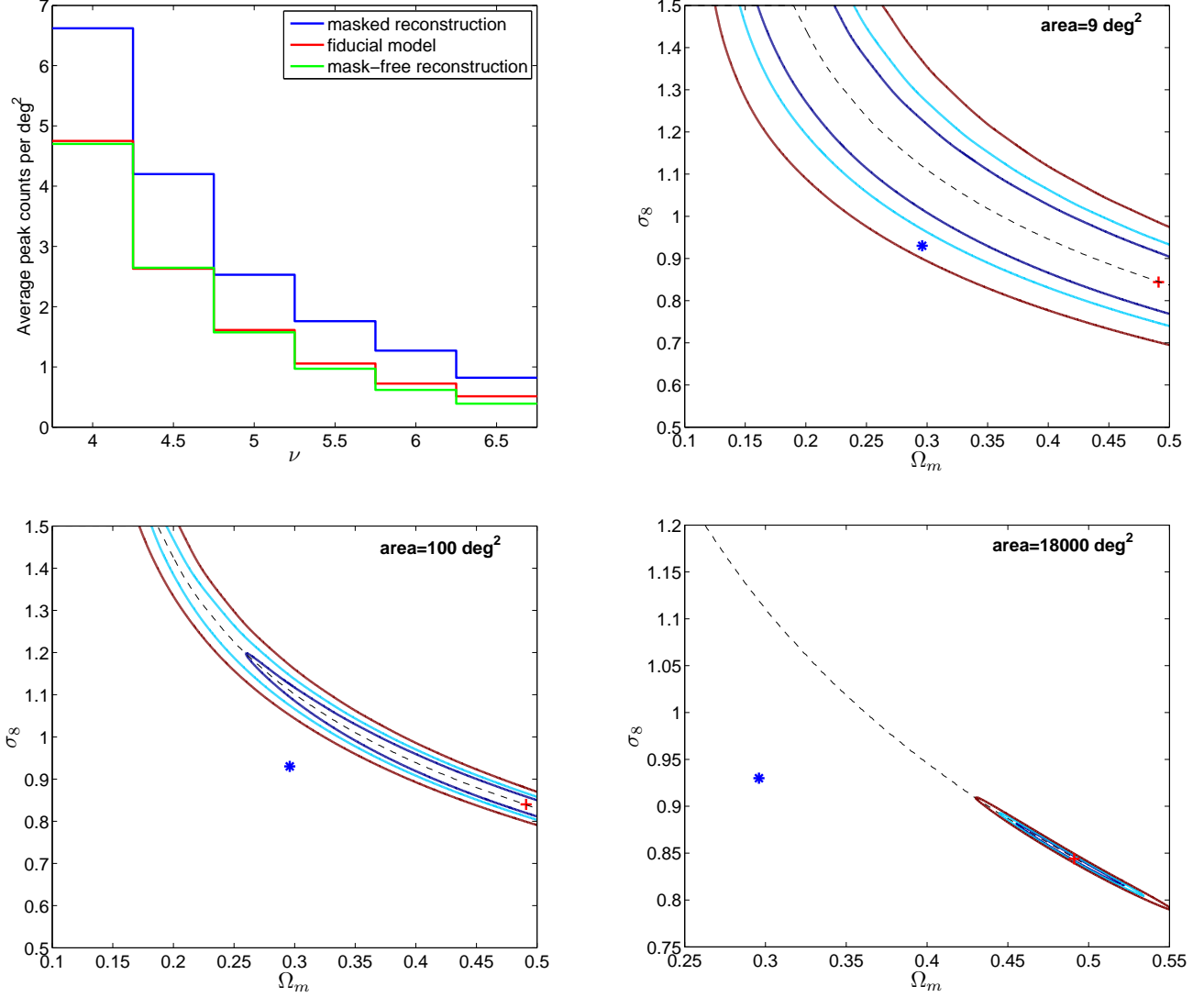


Figure 12. The bias in cosmological parameter constraints due to the mask effects. The upper left panel shows the peak number distribution where the blue, green and red histograms are for the cases with masks, without masks and the model prediction of Fan et al. (2010) with $\sigma_0 = 0.02$. The upper right panel shows the fitting results for the survey area of 9 deg^2 . The blue symbol is for the fiducial values and the red symbol is for the best fit with the peak counts in the case with masks as the 'observed data' and $\sigma_0 = 0.02$ in the model of Fan et al. (2010). The lower left and right panels are for the survey area of 100 deg^2 and 18000 deg^2 , respectively.

of the number of noise peaks given their peak heights measured in signal-to-noise ratio with σ_0 still be 0.02, the value in regions away from the masks. The later can be understood by noting that for any two-dimensional Gaussian random fields, their peak number density distributions are the same if the peak height is measured in signal-to-noise ratio with the noise level σ_0 different for different noise field (e.g., van Waerbeke 2000). Here for regions around masks, their true noise level is high. When counting peaks, however, we still use $\sigma_0 = 0.02$ (corresponding to $n_g = 30 \text{ arcmin}^{-2}$) uniformly to define the signal-to-noise ratio of peaks. Therefore the number density of peaks with high $\nu = K_N/\sigma_0$ ($\sigma_0 = 0.02$) is higher than that in regions away from masks. Based on these considerations, we develop a two-noise-level model that takes into account the lower number density of usable galaxies in regions around masks. Specifically, for each grid point, we calculate the effective contribution of different galaxies to it by

$$R^e = \frac{\sum_{k=1}^{N_{gal}} R u_k}{\sum_{k=1}^{N_{gal}} u_k}, \quad (27)$$

where $R = 1$ for galaxies outside masks and $R = 0$ for galaxies inside masks. The kernel u_k is the Gaussian smoothing function with $\theta_G = 1 \text{ arcmin}$, consistent with our analyses. We then obtain an effective number density of source galaxies at each grid point by

$$n_g^e = R^e n_g. \quad (28)$$

where $n_g = 30 \text{ arcmin}^{-2}$ here.

We divide the considered survey area into two parts, the regions around masks with 1.5 times of the mask size and the rest of the regions away from masks. They are named as, correspondingly, the mask affected regions and the nor-

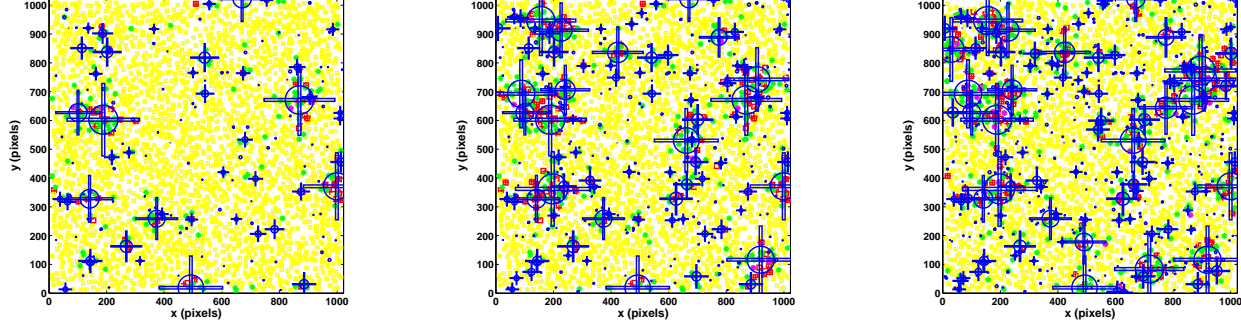


Figure 13. The illustration of the dependence of the mask effects on the masked fraction. From left to right, the masked area fraction is $\sim 6\%$, $\sim 13\%$, and $\sim 19\%$ ($N_{\text{mask}} = 140, 280$, and 420 in 9 deg^2), respectively. The meanings of the symbols are the same as those in the left panel of Figure 11.

Table 1
Mask effects on peak statistics with different mask fractions.

f_{mask}^a	N_{mask}^b	f_{nocorr}^c	f_{offset}^d	$f_{\nu > 3}^e$	$f_{m, \nu > 3}^f$	f_{LPin}^g	f_{NCin}^h	f_{LIinALL}^i
$\sim 6\%$	140	6.07%	24.56%	8.83%	10.88%	93.30%	71.52%	41.02%
$\sim 13\%$	280	10.76%	40.07%	9.01%	13.21%	93.50%	77.39%	44.40%
$\sim 19\%$	420	15.02%	52.25%	8.93%	15.76%	93.36%	82.60%	47.90%

^aMasked area fraction

^bNumber of masks in 9 deg^2

^cFraction of no-correspondence peaks among the total number of peaks

^dFraction of peaks with spatial offset larger than 0.1 arcmin .

^eFraction of peaks with $S/N > 3$ in the mask-free case

^fFraction of peaks with $S/N > 3$ in the case with masks

^gFraction of Type I affected peaks within regions around masks with a size of twice the corresponding masks among the total number of Type I affected peaks

^hFraction of no-correspondence peaks within regions of twice the size of masks among the total number of no-correspondence peaks

ⁱFraction of (Type I+Type II) affected peaks within regions of twice the size of masks among the total number of peaks within the regions

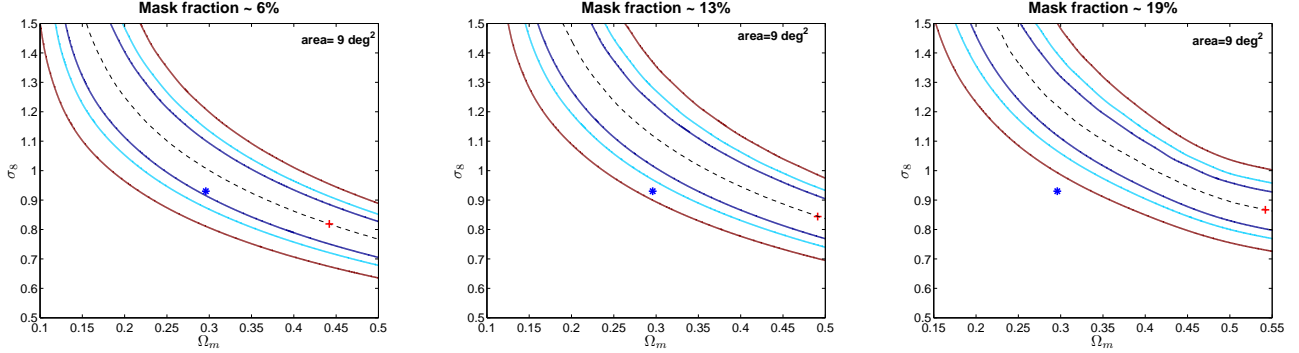


Figure 14. The corresponding results of cosmological constraints for different masked fractions shown in Figure 13.

mal regions. We calculate the effective number density of usable galaxies for the mask affected regions n_g^{emask} by averaging n_g^e of all the grid points within these regions. We obtain $n_g^{\text{emask}} \approx 13.7 \text{ arcmin}^{-2}$ for the case with the masked fraction of 13% considered here. For the normal regions, the effective number density n_g^{enorm} is calculated similarly by averaging all the grid points in the normal regions. We have $n_g^{\text{enorm}} \approx 29.3 \text{ arcmin}^{-2}$, very close to $n_g = 30 \text{ arcmin}^{-2}$ as expected. With these two effective number densities of galaxies, we calculate the number density of peaks separately for mask affected regions and for normal regions with the model of Fan et al. (2010). We then rescale the height for peaks by a uniform noise level $\sigma_0 = 0.02$, the value used in counting peaks from simulation maps. The theoretical predictions for the number of peaks in each S/N bin (with $\sigma_0 = 0.02$)

in the mask affected regions and normal regions are calculated by multiplying the corresponding areas of the two regions with their number densities of peaks. We then sum up the peak numbers in each bin in the two regions to obtain the total number of peaks in each bin. These theoretical predictions are then compared with the ‘observed’ numbers of peaks directly from the convergence maps with masks without any area exclusions. The results are shown in Figure 16 with the left panel for the peak counts and the right panel for the fitting results from our two-noise-level model. The blue, black and red histograms in the left panel correspond to the results from convergence maps in the case with masks directly, the theoretical prediction from the two-noise-level model, and the theoretical prediction from the model of Fan et al. (2010) with a uniform noise level of $\sigma_0 = 0.02$. Comparing to the upper right panel of Figure 12, the fitting results improve dra-

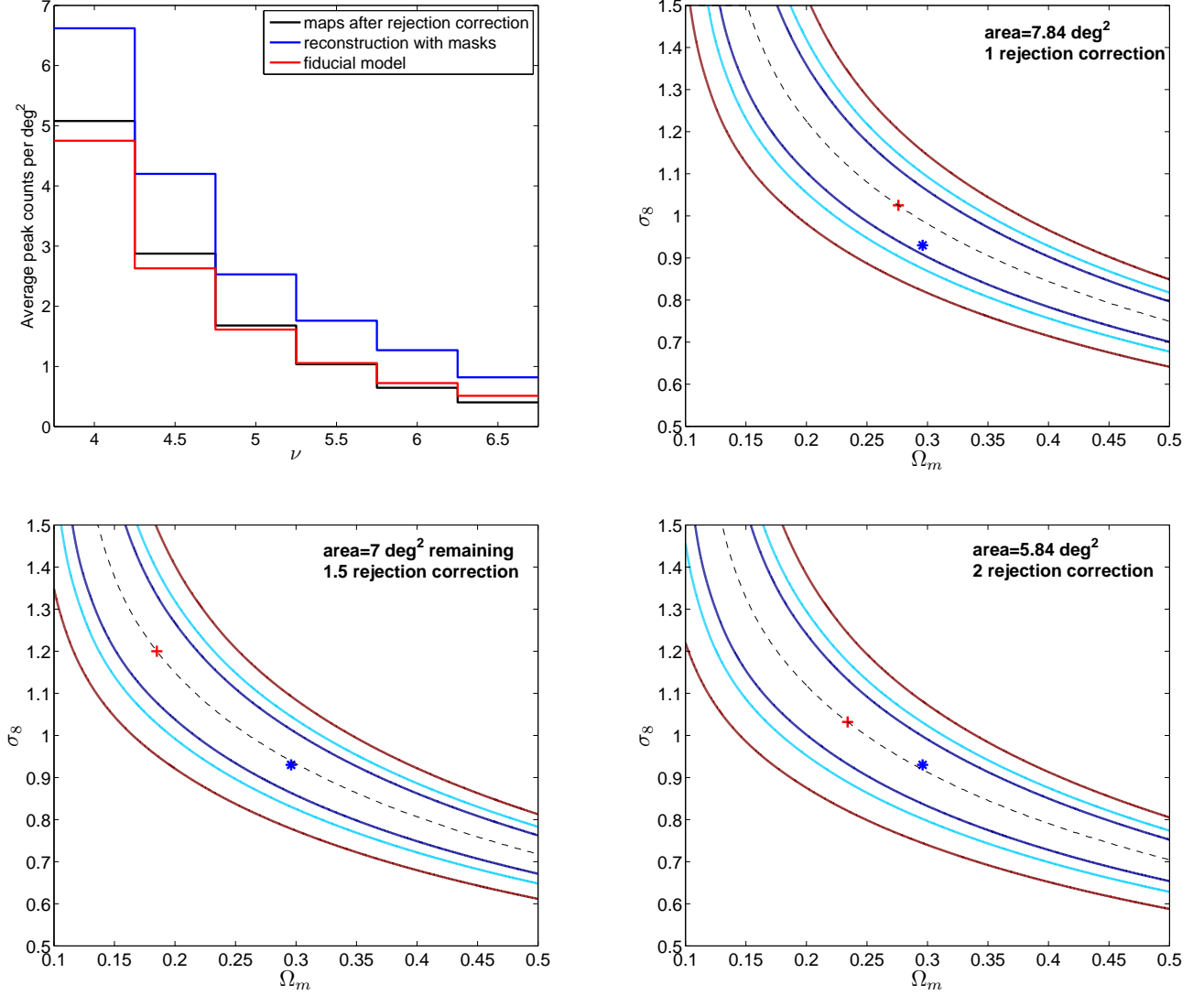


Figure 15. Results after rejection of regions around masks. The upper left panel shows the peak number distribution per deg^2 with the blue, black and red histograms for peak counts without rejection, with rejection of regions of 1.5 times the mask size around masks and the model prediction of Fan et al. (2010). The upper right panel shows the fitting results with the rejected regions equal to the masked regions. The lower left and right panels are the results for rejections of regions with 1.5 and 2 times of mask size, respectively. Here the number of masks is $N_{\text{peak}} = 280$ in 9 deg^2 and the corresponding masked fraction is 13%.

matically with a much reduced bias considering the parameter degeneracy along the dotted line. The best fit $\chi^2 \approx 0.16$ here while it is $\chi^2 \approx 6.64$ with the single noise model. The results show that our two-noise-model works very well and can potentially be applied in cosmological studies with weak lensing peak counts in the presence of masks.

5. SUMMARY AND DISCUSSION

In this paper, we analyze the mask effects on weak lensing convergence peak statistics and the consequent cosmological parameter constraints from weak lensing peak counts. Along the way, we also study different effects arising from convergence reconstructions from measured ellipticities of source galaxies. Our base convergence and shear maps are taken from White & Vale (2004) with the source redshift $z_s = 1$. We generate source galaxy catalogs by randomly populating galaxies on the source plane with $n_g = 30 \text{ arcmin}^{-2}$. A random intrinsic ellipticity based on the truncated Gaussian dis-

tribution with the total $\sigma_\epsilon = 0.4$ is assigned to each galaxy. The mask catalogs are produced according to the mask size distribution of CFHTLS. To perform statistical analyses, for each of the 32 base weak lensing simulations, we generate 5 noisy maps without/with masks with different assigned intrinsic ellipticities and different masks in the masked case. We therefore have totally 160 convergence maps for each case. We use the theoretical model of Fan et al. (2010) for weak lensing peak counts to analyze the cosmological parameter constraints in different cases. The model takes into account fully the noise effects arising from intrinsic ellipticities so that we can use directly peaks from convergence maps in cosmological studies without the need to find true peaks associated with clusters of galaxies. We test the model applicability with the ‘observed data’ from simulations without masks and find that the derived cosmological parameters agree with the fiducial input of the simulations very well without significant bias.

Our main results are summarized as follows.

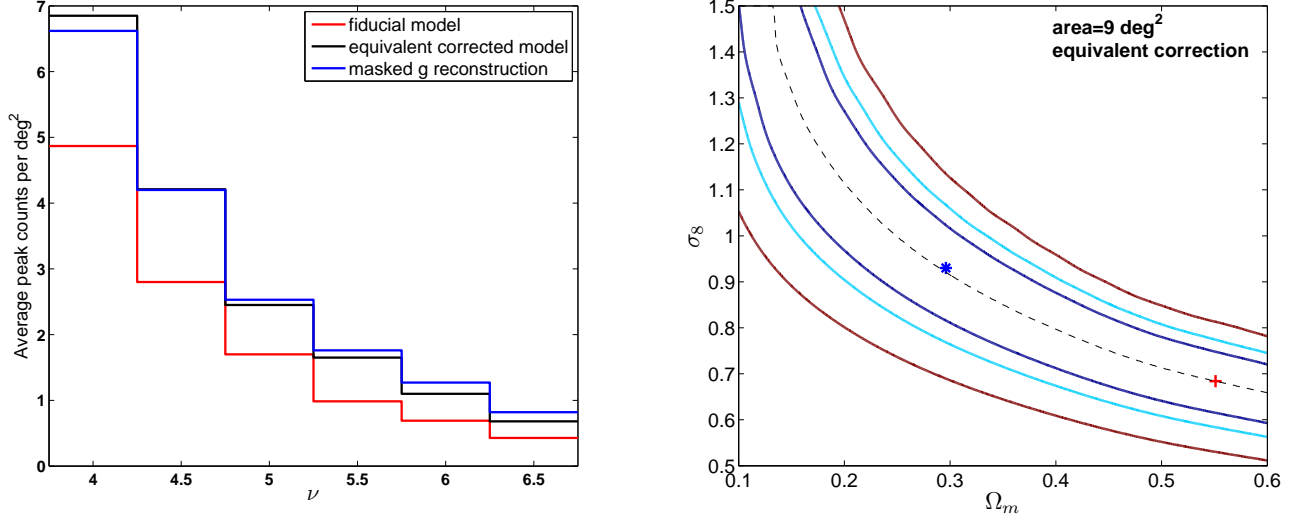


Figure 16. Left: Cosmological constraints for $\sim 13\%$ masked g reconstruction after equivalent correction. Same notation as upper-right panel of Fig 2. Right: Average peak height distribution for masked g reconstruction (blue), equivalent corrected model (black) and fiducial model prediction (red).

(1) Because of the difference between the smoothed $\langle g \rangle$ and $\langle \gamma \rangle / (1 - \langle \kappa \rangle)$, the smoothing procedure in g reconstruction leads to the reconstructed convergence systematically lower than the true smoothed convergence in dark matter halo regions. This can affect the weak lensing peak counts, which should be considered carefully, especially for future studies with large surveys.

(2) The mass-sheet degeneracy problem in convergence reconstructions can affect the covariance matrix of peak counts, which in turn affects the confidence range of cosmological parameter constraints. It is expected that with the increase of the area in reconstruction, this effect in covariance matrix should decrease.

(3) The occurrence of masked regions reduces the number of usable source galaxies and therefore increases the noise in the regions around masks. This in turn leads to systematic increases of the number of high peaks and consequently a significant bias in cosmological parameters constrained from weak lensing peak counts. The larger the masked area fraction is, the larger the effects are.

(4) We find that the significantly affected region around a mask is about 1.5 times of the mask size. Excluding such regions in peak counting can eliminate largely the mask effects and reduce the bias in cosmological parameters derived from weak lensing peak abundance significantly.

(5) We develop a two-noise-level model that treats the mask affected regions separately. This model can account for the mask effects on weak lensing peak counts very well. The derived cosmological parameters based on this model improve dramatically comparing to the large bias from the model with a uniform noise.

In our analyses, we apply the Kaiser-Squires method with the nonlinear reduced shear in the convergence reconstruction. For the maximum-likelihood reconstruction method (Bartelmann et al. 1996), we expect that the mask effects on the reconstructed convergence field and the peak counts are qualitatively similar to the results shown in this paper although quantitative studies are still needed. For other methods, such as the multi-scale entropy restoration filtering, namely MRLens (Starck et al. 2006), the mask effects can be

different and detailed analyses should be carried out when a specific reconstruction method is used.

We note that the two-noise-level model works well to take into account the mask effects on weak lensing peak counts. Detailed inspection finds, however, that the model prediction for the dependence of peak counts on the peak height is slightly steeper than that from simulations. To improve the model, we may need to treat the mask affected regions more accurately by further dividing them into different sub-regions with different noise levels. We will investigate along this line of approach thoroughly in the future.

6. ACKNOWLEDGEMENT

We are thankful for the discussions with David Wittman that stimulate the studies on the mask effects and with Huanyuan Shan. We appreciate Martin White for kindly making the weak lensing simulation data publicly available. This research is supported in part by the NSFC of China under grants 11173001 and 11033005, and the 973 program No. 2007CB815401.

REFERENCES

- Abate, A., Aldering, G., Allen, S. W., et al., 2012, arXiv:1211.0310
- Albrecht, A., et al., 2006, arXiv:astro-ph/0609591
- Amara, A., & Refregier, A., 2008, MNRAS, 391, 228
- Amendola, L., Appleby, S., Bacon, D., et al., 2012, arXiv:1206.1225
- Bartelmann, M., 1995, A&A, 303, 643
- Bartelmann, M., Narayan, R., Seitz, S., & Schneider, P., 1996, ApJ, 464, L115
- Bartelmann M., Schneider P., 2001, Phys. Rep., 340, 291
- Bridle, S., & King, L. J., 2007, NewJ.Phys., 9, 444
- Bryan, G. L., & Norman, M. L., 1998, ApJ, 495, 80
- Bullock, J. S., et al., 2001, MNRAS, 321, 559
- Carroll, S. M., Press, W. H., & Turner, E. L., 1992, ARA&A, 30, 499
- Dietrich, J. P., & Hartlap, J., 2010, MNRAS, 402, 1049
- Eisenstein, D. J., & Hu, W., 1998, ApJ, 496, 605
- Eisenstein, D. J., & Hu, W., 1999, ApJ, 511, 5
- Erben, T., Hildebrandt, H., Miller, L., et al., 2012, arXiv:1210.8156
- Fan, Z. H., 2007, ApJ, 669, 10
- Fan, Z. H., Shan, H. Y., & Liu, J. Y., 2010, ApJ, 719, 1408
- Gavazzi, R., & Soucail, G., 2007, A&A, 464, 399
- Hamana, T., Takada, M., & Yoshida, N., 2004, MNRAS, 350, 893
- Hamana, T., Oguri, M., Masato, S., & Sato, M., 2012, MNRAS, 425, 228
- Hennawi, J. F., & Spergel, D. N., 2005, ApJ, 624, 59
- Heymans, C., Van Waerbeke, L., Miller, L., et al., 2012, MNRAS, 427, 146
- Hikage, C., Takada, M., Hamana, T., & Spergel, D., 2011, MNRAS, 412, 65

- Hilbert, S., Marian, L., Smith, R. E., & Desjacques, V., 2012, MNRAS, 426, 2870
- Hinshaw, G., Larson, D., Komatsu, E., et al., 2012, arXiv:1212.5226
- Hoekstra, H., & Jain, B., 2008, Annual Review of Nuclear and Particle Science, 58, 99
- Hoekstra, H., Yee, H. K. C., Gladders, M. D., 2002, New Astro. Rev., 46, 767
- Kaiser, N. & Squires, G., 1993, ApJ, 404, 441
- Kilbinger, M., Fu, L. P., Heymans, C., et al., 2012, arXiv:1212.3338
- Komatsu, E., Smith, K. M., Dunkley, J., et al., 2011, ApJS, 192, 18
- Kratochvil, J. M., Haiman, Z., & May, M., 2010, Phys. Rev. D, 81, 043519
- Ma, Z., Hu, W., & Huterer, D., 2006, ApJ, 636, 21
- Marian, L., Smith, R. E., & Bernstein, G. M., 2009, ApJ, 698, L33
- Marian, L., Smith, R. E., Hilbert, S., Schneider, P., 2012, MNRAS, 423, 1711
- Munshi, D., et al., 2008, Phys. Rep., 462, 67
- Navarro, J., Frenk, C., & White, S. D. M., 1996, ApJ, 462, 563
- Navarro, J., Frenk, C., & White, S. D. M., 1997, ApJ, 490, 493
- Schirmer, M., Erben, T., Hettterscheidt, M., & Schneider, P., 2007, A&A, 462, 875
- Schneider, P. & Seitz, C., 1995, A&A, 294, 411
- Seitz, C. & Schneider, P., 1997, A&A, 318, 687
- Shan, H. Y., Kneib, J. P., Tao, C., et al., 2012, ApJ, 748, 56
- Sheth, R. K., & Tormen, G., 1999, MNRAS, 308, 119
- Simpson, F., Heymans, C., Parkinson, D., et al., 2012, MNRAS (in press), arXiv:1212.3339
- Spergel, D. N., et al., 2003, ApJS, 148, 175
- Starck, J. L., Pires, S., & Refregier, A., 2006, A&A, 451, 1139
- Sun, L., Fan, Z. H., Tao, C., Kneib, J.-P., Jouvel, S., & Tilquin, A., 2009, ApJ, 699, 958
- Takada M., & Jain B., 2003, MNRAS, 340, 580
- Tang, J. Y., & Fan, Z. H., 2005, ApJ, 635, 60
- van Waerbeke, L., 2000, MNRAS, 313, 524
- van Waerbeke, L., Mellier Y. & Hoekstra H., 2005, A&A, 429, 75
- von der Linden, A., Erben, T., Schneider, P., & Castander, F. J., 2006, A&A, 454, 37
- Wang, S., Haiman, Z., & May, M., 2009, ApJ, 691, 547
- White, M., van Waerbeke, L., & Mackey, J., 2002, ApJ, 575, 640
- White, M., & Vale, C., 2004, Astropart.Phys, 22, 27
- Wittman, D., Dell'Antonio, I. P., Hughes, J. P., et al., 2006, ApJ, 643, 128
- Yang, X. J., Kratochvil, J. M., Wang, S., Lim, E. A., Haiman, Z., May, M., 2011, Phys. Rev. D., 84, 043529
- Yang, X. J., Kratochvil, J. M., Haffenberger, K., Haiman, Z., & May, M., 2012, arXiv:1210.0608